Fermi National Accelerator Laboratory

FERMILAB-Conf-96/006

Target and Collection Optimization for Muon Colliders

N.V. Mokhov, R.J. Noble and A. Van Ginneken

Fermi National Accelerator Laboratory
P.O. Box 500, Batavia, Illinois 60510

January 1996

Proceedings of the *9th Advanced ICFA Beam Dynamics Workshop: Beam Dynamics and Technology Issues for $\mu^+\mu^-$ Colliders*, Montauk, New York, Oct.15-20, 1995.

Operated by Universities Research Association Inc. under Contract No. DE-AC02-76CHO3000 with the United States Department of Energy

Target and Collection Optimization for Muon Colliders

N. V. Mokhov, R. J. Noble and A. Van Ginneken

*Fermi National Accelerator Laboratory**

P.O. Box 500, Batavia, Illinois 60510

January 10, 1996

Abstract

To achieve adequate luminosity in a muon collider it is necessary to produce and collect large numbers of muons. The basic method used in this paper follows closely a proposed scheme which starts with a proton beam impinging on a thick target ($\sim$ one interaction length) followed by a long solenoid which collects muons resulting mainly from pion decay. Production and collection of pions and their decay muons must be optimized while keeping in mind limitations of target integrity and of the technology of magnets and cavities. Results of extensive simulations for 8 GeV protons on various targets and with various collection schemes are reported. Besides muon yields results include energy deposition in target and solenoid to address cooling requirements for these systems. Target composition, diameter, and length are varied in this study as well as the configuration and field strengths of the solenoid channnel. A *curved* solenoid field is introduced to separate positive and negative pions within a few meters of the target. This permits each to be placed in separate RF buckets for acceleration which effectively doubles the number of muons per bunch available for collisions and increases the luminosity fourfold.

*To be published by AIP in *Proceedings of the 9th Advanced ICFA Beam Dynamics Workshop: Beam Dynamics and Technology Issues for $\mu^+\mu^-$ Colliders*, Montauk, NY, October 15-20, 1995

INTRODUCTION

Interest in a muon collider for future high energy physics experiments has greatly increased recently [1]. Muons suffer far less synchrotron radiation than electrons providing hope that well-known circular machine technology can be extended to much higher energies than presently available—or even contemplated—for lepton colliders. The short muon lifetime and the difficulty and expense of producing large numbers of them makes a useful muon collider luminosity hard to achieve. Because of their short lifetime muons must be generated by a single proton pulse for each new acceleration cycle. Techniques for efficient production and collection of an adequate number of muons are thus needed to make a muon collider viable.

Earlier estimates of muon yield, based on conventional lithium lens and quadrupole magnet collection methods, indicate that roughly 1000 protons are needed for every muon delivered to the collider rings [2]. This results from inherent limitations in the momentum acceptance of these systems (typically less than ± 5 percent) which causes most (potential) muons produced to be wasted.

Motivated by neutrino beamline experience, a solenoid collection scheme for pions has been suggested [3]. Cursory simulations indicate significant improvement in muon yields for proton energies below 100 GeV while above this a collection system with two lithium lenses could surpass a solenoid. However the power required for a 15 to 30 Hz rapid-cycling proton synchrotron with 10^{14} protons per pulse becomes expensive above 30 GeV. Along with considerations on space charge limits and pion yields this suggests a kinetic energy of the proton driver between 3 and 30 GeV. Because of interest at Fermilab in upgrading its 15 Hz Booster to higher intensity (5×10^{13} protons per pulse) for the hadron program, a proton beam kinetic energy of 8 GeV is assumed in this study. This choice also might enable experimental verification of results presented here. Actual *numbers* reported here, such as yields and energy densities, may well depend considerably on incident energy. But *intercomparisons* and conclusions derived from them, such as in the optimization of target size or solenoid field with respect to muon yield, are expected to be much less sensitive to incident energy.

The basic collection scheme, as outlined by Palmer et al. [3], is illustrated in Fig. 1 and forms the starting point for the simulations described in this paper. A very high-field hybrid solenoid extends the length of a target upon which a proton beam impinges. Based on near term technology, a field of 28 T and a 7.5 cm radius appears to be achievable for this purpose. This target solenoid collects pions with a large momentum spread and with large angles and guides them downstream into a long 7 T solenoid channel (15 cm radius) where they decay to muons.

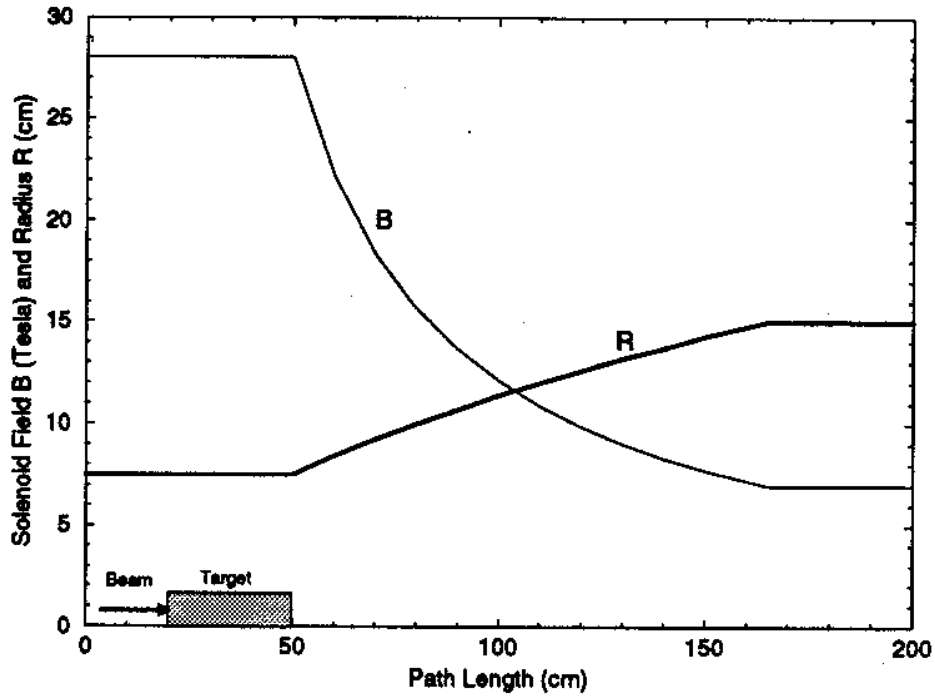

FIGURE 1. Capture solenoid field and inner radius as a function of distance.

The high-field solenoid aperture is chosen to have a large transverse phase space acceptance adequate for a transverse momentum

$$p_{\perp}^{max} = qBa/2 = 0.314\ GeV/c \tag{1}$$

where B is the magnetic field, q the particle charge, and a the solenoid radius. The normalized acceptance of this solenoid for pions is

$$A_n = ap_{\perp}^{max}/\ m_{\pi}c = qBa^2/2m_{\pi}c. \tag{2}$$

For the given parameters this acceptance is 0.17 m·rad, which is much larger than the intrinsic pion beam emittance at the target, $r_p p_{\perp}^{max}/m_{\pi}c = 0.02$ m·rad for a proton beam radius r_p. Hence there is no reason to further reduce proton beam size—which may thus be set by considerations of yield and target heating rather than pion emittance.

The target region is followed immediately by a 115 cm long matching section which reduces the field to 7 T via a $B_0/(1+\alpha z)$ dependence. In this region the pipe radius increases from 7.5 to 15 cm which corresponds to the radius of the lower field solenoid serving as pion decay region. This keeps the product Ba^2 constant and the acceptance unchanged. The parameter $\alpha = (qB_0/2p_{\pi})(d\beta_f/dz)$ is chosen such that for a characteristic pion momentum the rate of change of the beta focusing function

($\beta_f = 2p_\pi/qB$) with distance is less than 0.5, which might still be considered an adiabatic change of the field. In the present case $p_\pi = 0.8$ GeV/c and α =2.62 m^{-1} are chosen.

Below, following a brief description of computational procedures, results are presented on energy deposition in the targets and surrounding solenoid and on pion and muon production from various targets. Next, dependence of yield on the parameters specifying the decay channel solenoids is examined. This includes introduction of a *curved* solenoid to separate particle species by charge downstream. Concluding remarks are in the final section.

TARGET REGION STUDIES

For the collection geometry described in the Introduction, target composition, length and radius are varied and pion yield is studied using particle production and transport simulation codes. The 8 GeVproton beam is assumed to have an emittance of $\epsilon_N^{rms} = 3.8 \times 10^{-5}$ m·rad consistent with a value expected from a high-intensity proton source. The focusing function at the target is conservatively chosen as $\beta^* = 4$ meters to result in a relatively wide beam with $\sigma(x) = \sigma(y) = 0.4$ cm and $\sigma(x') = \sigma(y') = 1$ mrad.

Two computer codes are used in this study. The code MARS [4], developed over many years at IHEP and Fermilab for particle–matter interaction simulations, is used for simulating particle production and transport in thick targets within the solenoid field. MARS is also used to study energy deposition in the target and surrounding solenoid. Calculated pion, kaon, and proton spectra at the target exit for a representative case are shown in Fig. 2. MARS describes all the physics processes, so particle decay, interaction, and transport down the solenoid channel can be simulated within MARS as well. It is found preferable in this case to write a special, fast code for tracking particles after the target, using as input a particle file generated by MARS at the end of the target.

This code keeps track of vectorial positions and momenta of each particle as it traverses the beamline as well as time elapsed since the arrival of the incident proton at the target. In addition the code performs $\pi/K \rightarrow \mu$ decay Monte Carlo selection and full kinematics. Muons are progressively downweighted by their decay probability as they traverse the channel. Pions and muons leaving the beampipe are considered lost. In principle there is a small (but presumably negligible) fraction which may scatter back out of the wall or—in the case of a pion—produce a secondary pion which may rejoin the beam. Debuncher cavities for reducing pion/muon momentum spread downstream of the target are at present not included in the simulations but are planned to be added at a later date.

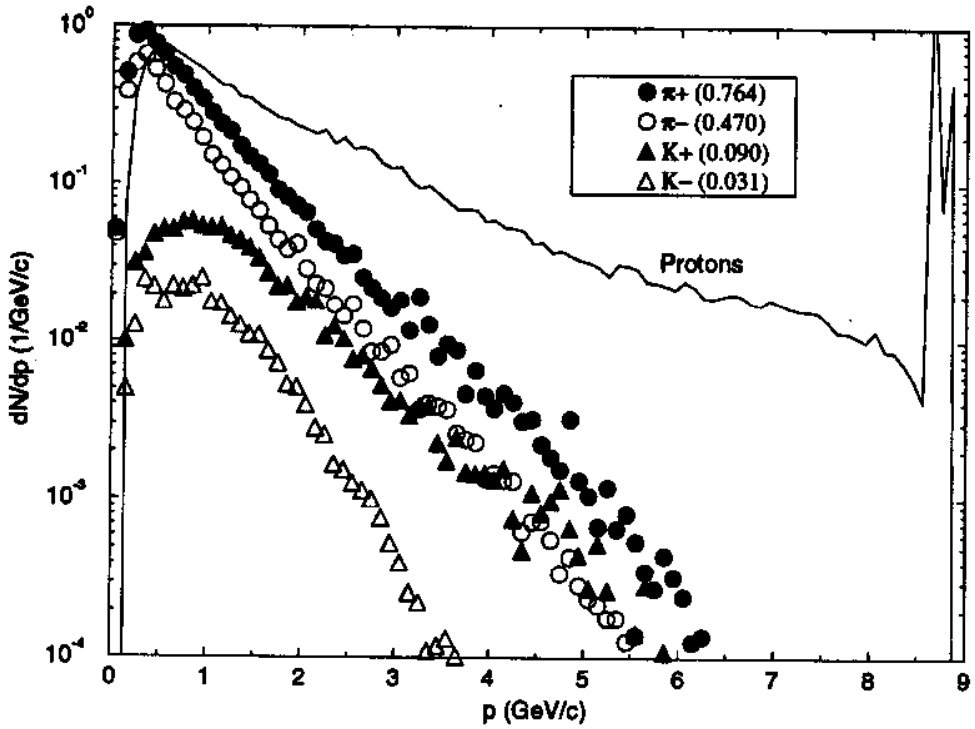

FIGURE 2. Pion, kaon and proton spectra for 8 GeV protons incident on a copper target (1.5 λ length, 1 cm radius). Total meson yields are shown in parentheses.

A large variety of particles is produced by the 8 GeV protons and subsequently by secondary and higher generation particles. For 8 GeV p–p interactions the average charged particle multiplicity is about three [5] with a modest increase expected for p–nucleus collisions. Excluding the incident protons this leaves an average of somewhat in excess of one charged particle produced per interaction—mostly as pions. Of all produced pions one expects roughly one third to be π^0 which decay quickly into γs leading to electromagnetic cascades in the target. For heavier targets the shorter radiation length permits considerable growth of these cascades leading to many low energy electrons and photons. Among the outgoing particles there will also be some nucleons and nuclear fragments which are dislodged from the target nuclei. All these processes are represented in the MARS code along with elastic and quasi elastic scattering of incident and produced particles.

Simulation of π/μ transport in constant solenoidal fields is readily performed using exact helical trajectories. In the matching region, where the field is more complicated, the simulation proceeds by taking small steps (0.1–0.5 cm) and sampling the field along the trajectory. The declining field in the matching region means that according to the $\nabla \cdot \boldsymbol{B} = 0$ condition the field has a radial component: $B_r \simeq -\frac{1}{2} r \partial B_z / \partial z$. For the above z-dependence $\partial B_r / \partial z = -\frac{1}{2} r \partial^2 B_z / \partial z^2 \neq 0$ and it follows [6] from the $\nabla \times \boldsymbol{B} = 0$ condition that B_z must depend on r. This requires

that an extra term be present in B_z which—in turn—requires (via $\nabla \cdot \boldsymbol{B} = 0$) an extra term in B_r, etc. For the present simulations the iteration is pursued up to quadratic correction terms:

$$
\begin{aligned}
B_z &= \frac{B_0}{1+\alpha z}\left[1-\frac{1}{2}\left(\frac{\alpha r}{1+\alpha z}\right)^2\right] \\
B_r &= \frac{B_0 \alpha r}{2(1+\alpha z)^2}\left[1-\frac{3}{4}\left(\frac{\alpha r}{1+\alpha z}\right)^2\right].
\end{aligned} \tag{3}
$$

It should be remarked that the analysis simplifies considerably if B_z is made to decline *linearly* with distance in the matching region: $B_z = B_0(1-az)$. Then $B_r = \frac{1}{2} r a B_0$ independent of z and both $\nabla \cdot \boldsymbol{B} = 0$ and $\nabla \times \boldsymbol{B} = 0$ are satisfied. Results of simulations performed with a linear field do not differ significantly from those obtained with the $(1+\alpha z)^{-1}$–dependence.

Target Optimization

A crude target optimization with respect to yield starts by 'tagging' those pions (and kaons) which result in an acceptable muon deep in the decay channel for the case of a copper target followed by the 'standard' geometry as described in the Introduction (see Fig. 1). In excess of 90% of all accepted muons are thus shown to be the progeny of pions in the momentum range 0.2–2.5 GeV/c. The π^+/π^- ratio is about 1.6 at this proton energy. Then for a series of MARS runs, *pion* yield in the above momentum range is determined for various target parameters—without simulation of the collection channel. In addition to contributing little to the muon yield, pions with momenta less than 0.2 GeV/c have velocities below 0.82c and thus will quickly drop far behind the main pulse of faster particles.

Fig. 3(a–c) show momentum versus time scatter plots of pions, kaons and muons for a proton beam with $\sigma_t = 3$ nsec incident on a 22.5 cm copper target. In Fig. 3a the π/K distributions are shown immediately after the target and in Figs. 3b and 3c the π/K and μ distributions are shown 25 meters downstream of the end of the target. In all plots $t = 0$ refers to the center of the proton bunch at the target entrance. Materials investigated as target candidates are carbon, aluminum, copper, tungsten, and iridium. This set spans the Periodic Table and ranges in density from 1.8 to 22.4 g/cm^3. It is found that the optimal target radius needed to maximize the pion yield is about 2.5 times the rms beam size for all target materials and lengths. This corresponds to a 1 cm radius target for the beam used in this study. Almost all studies reported here are carried out with this target radius.

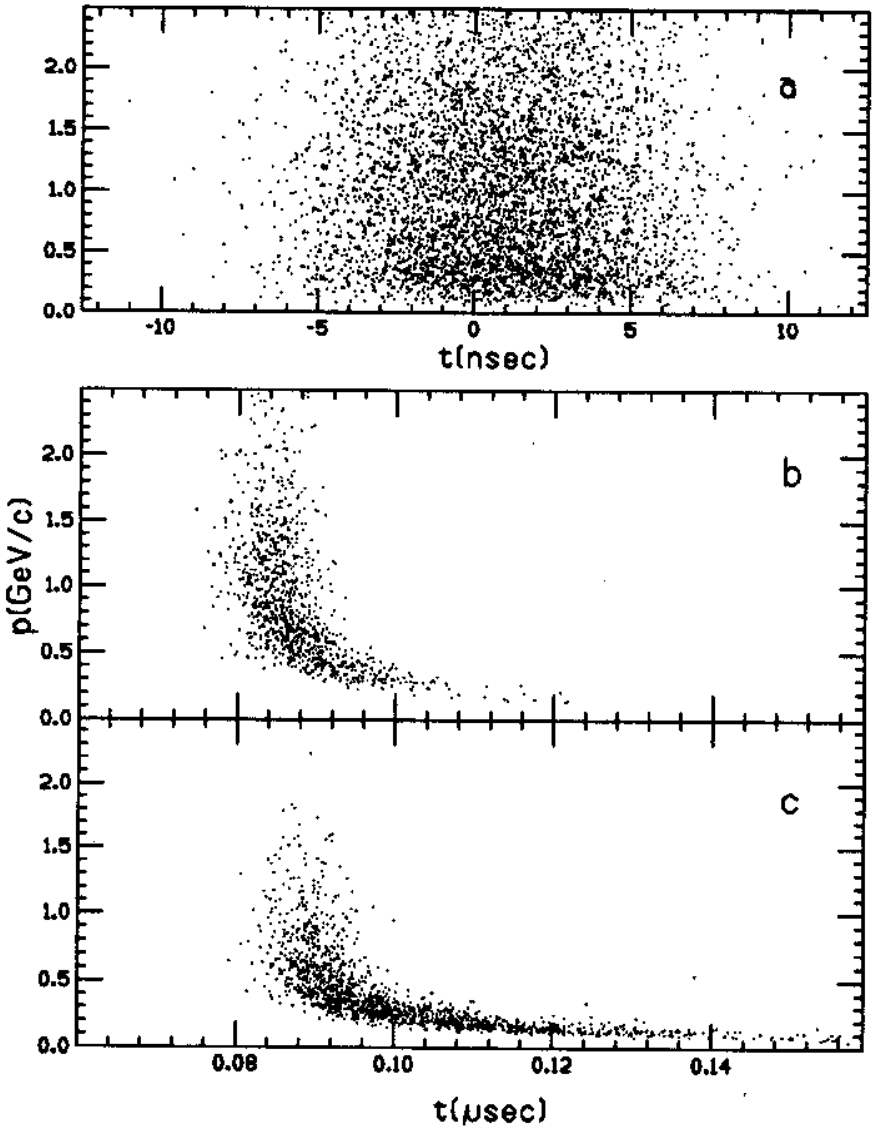

FIGURE 3. (a) π and K momentum *vs* time distribution immediately after the target for 8 GeV proton beam with $\sigma_t = 3$ nsec. (b) π and K distributions 25 meters downstream of target. (c) μ distribution 25 meters downstream of target.

Target length is varied from 0.5 to 2.5 nuclear interaction lengths (λ_I). Figs. 4 and 5 show positive and negative pion yields at the target exit as a function of target length for four materials (W and Ir are nearly identical). Optimal length is about 1.5 λ_I but yields vary by no more than 10% over a range of 1 to 2.5 λ_I for any target material. Yields are also rather insensitive with respect to target composition. The maximum yield is observed for a (1.5 $\lambda_I = 22.5$ cm) copper target, but the low–Z materials produce only $\approx$ 20% less.

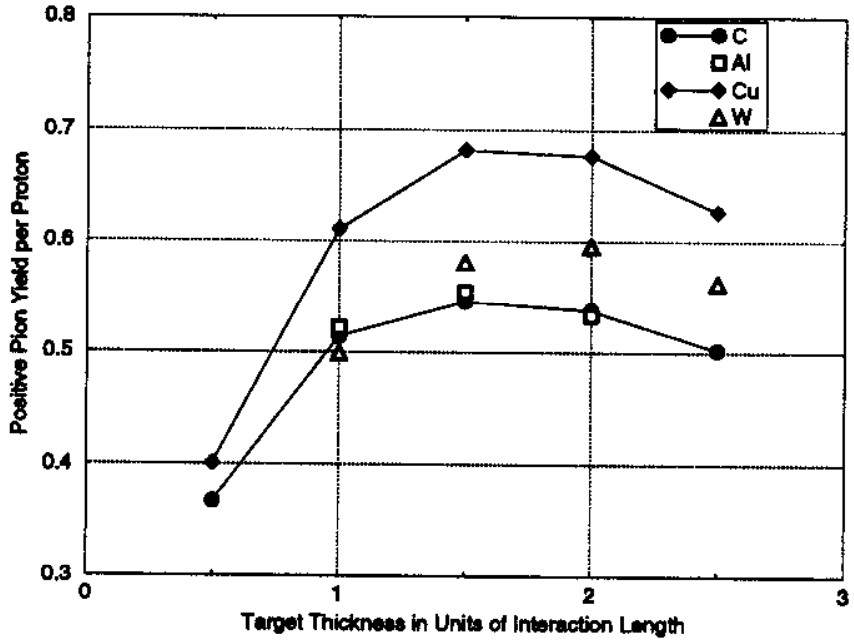

FIGURE 4. π^+ yield per 8 GeV proton for 1 cm radius targets of various materials *vs* target length for π momenta of $0.2 \leq p \leq 2.5$ GeV/c.

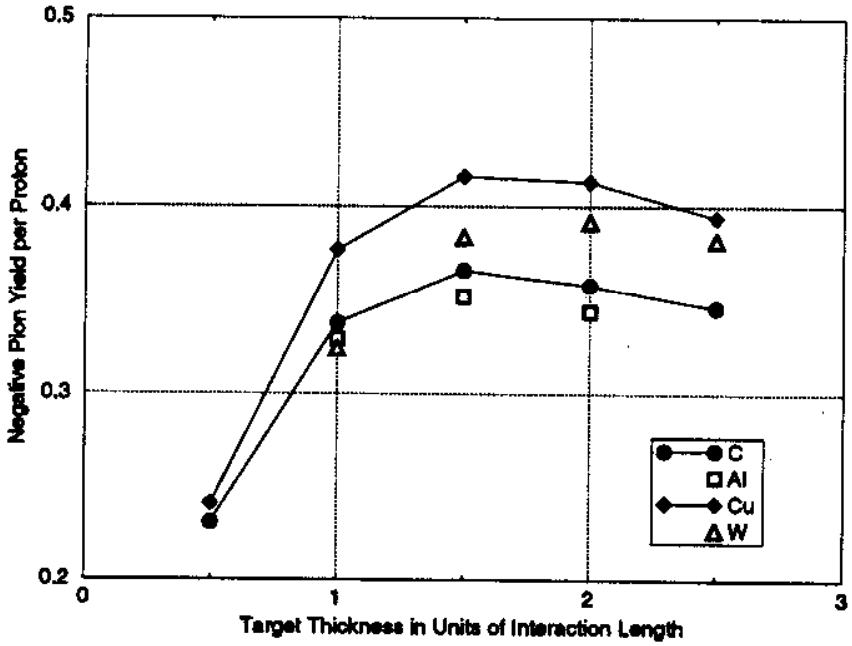

FIGURE 5. π^- yield per 8 GeV proton for 1 cm radius targets of various materials *vs* target length for π momenta of $0.2 \leq p \leq 2.5$ GeV/c.

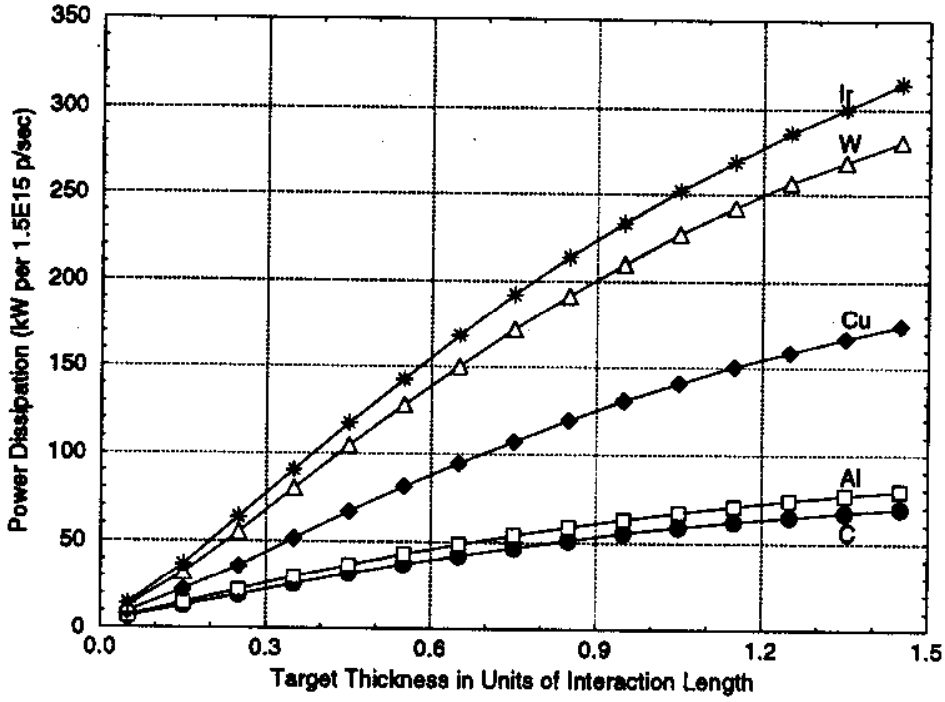

FIGURE 6. Average power dissipation in different 1 cm radius targets due to 8 GeV incident beam of 5×10^{13} protons at 30 Hz.

Target Heating

Beam power deposited in the target varies greatly with composition due mainly to increased electromagnetic shower development in high-Z materials. With 5×10^{13} protons on a 1.5 λ_I, 1 cm radius target, average power dissipation at 30 Hz ranges from 0.39 kW/cm^3 in carbon to 7.6 kW/cm^3 in iridium (Fig. 6). Peak energy deposition (on axis) in the target ranges from 20 J/g (C) to 35 J/g (Ir). This is at least a factor of ten below the shock damage limit. For forced water cooling of solid targets, the maximum surface heat flux (ϕ_{max}) that can be practically removed is about 200 W/cm^3. This implies a maximum target radius r=$2\phi_{max}/P$ where P is the average power density in W/cm^3. Hence—at 30 Hz—a (1 cm radius) carbon or aluminum target appears a viable candidate with proper cooling. Copper or other high-Z targets probably need to have a larger radius at this beam intensity to lower the power density. Alternatively, at high power densities one may resort to 'microchannel' cooling wherein target wires are interspersed with small diameter cooling channels.

Another option to alleviate target heating problems is to use elliptically shaped beams on matching targets. This has two advantages: the overall surface area accessible to cooling is increased while the distance from the point of maximum energy density to a cooled surface is decreased. There are some disadvantages connected with preparation of the elliptic beam and with target alignment—particularly

for large aspect ratios. Details of this are not further pursued here beyond a brief investigation which compares a round copper target of 1.5 λ_I and 1 cm radius with an elliptical one of equal length measuring 0.25 and 4 cm along the axes. The beam is likewise deformed in the same aspect ratio but retains the same emittance as for the 'round' case. As is confirmed by the simulations this has little effect on either maximum or total energy deposition or on yield. In this example total surface area increases by a factor of about 2.5 while distance between maximum energy deposition and cooling surface decreases by a factor of four.

Fig. 7 shows maximum temperature rise $\Delta T = T - T_0$ relative to room temperature $T_0 = 27°C$ reached in copper and carbon targets 1.5 λ_I long and 1 cm in radius when irradiated with 8 GeV protons. Results are obtained with the ANSYS code [7] starting with energy deposition distributions generated by MARS. Ideal cooling with $\Delta T = 0$ at r=1 cm is assumed. Equilibrium is approached in less than two seconds with a steady-state temperature at the maximum of 347°C in copper and 186°C in carbon. Equilibrium temperature rise versus depth z in the target for a set of $\Delta r = 0.2$ cm radial increments is shown in Fig. 8. Below, a 1.5 λ_I, 1 cm radius copper target is used in many instances. In view of the weak dependence of yield on target-Z almost all results pertaining to particle yield—*not* energy deposition—obtained with this target are expected to apply to carbon or aluminum with minor adjustments.

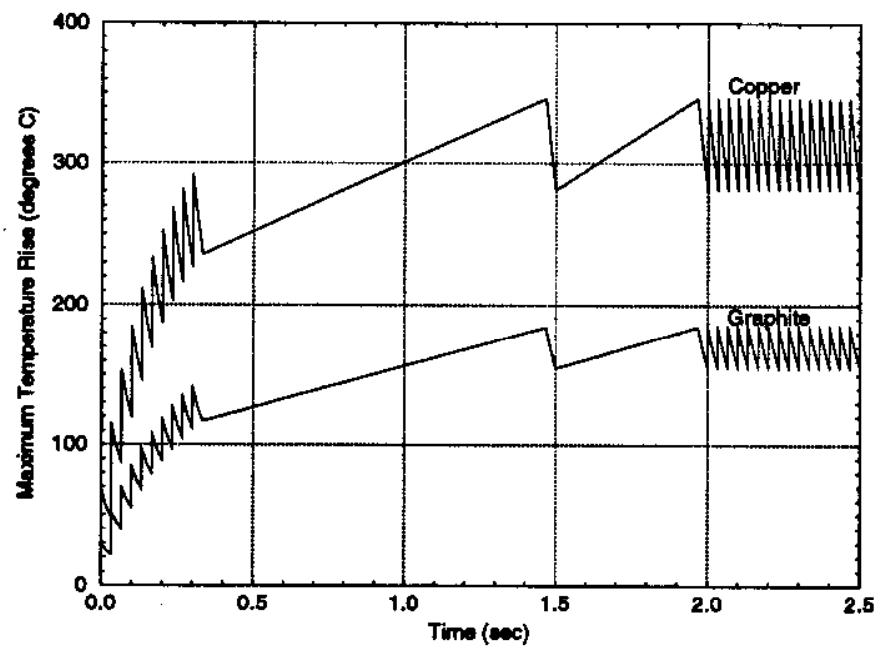

FIGURE 7. Maximum temperature rise ΔT relative to room temperature $T_0 = 27°C$ in 1 cm radius copper and graphite targets when irradiated by 8 GeV beam of 5×10^{13} protons at 30 Hz. ΔT for times between 0.3 and 2 sec is not shown in detail.

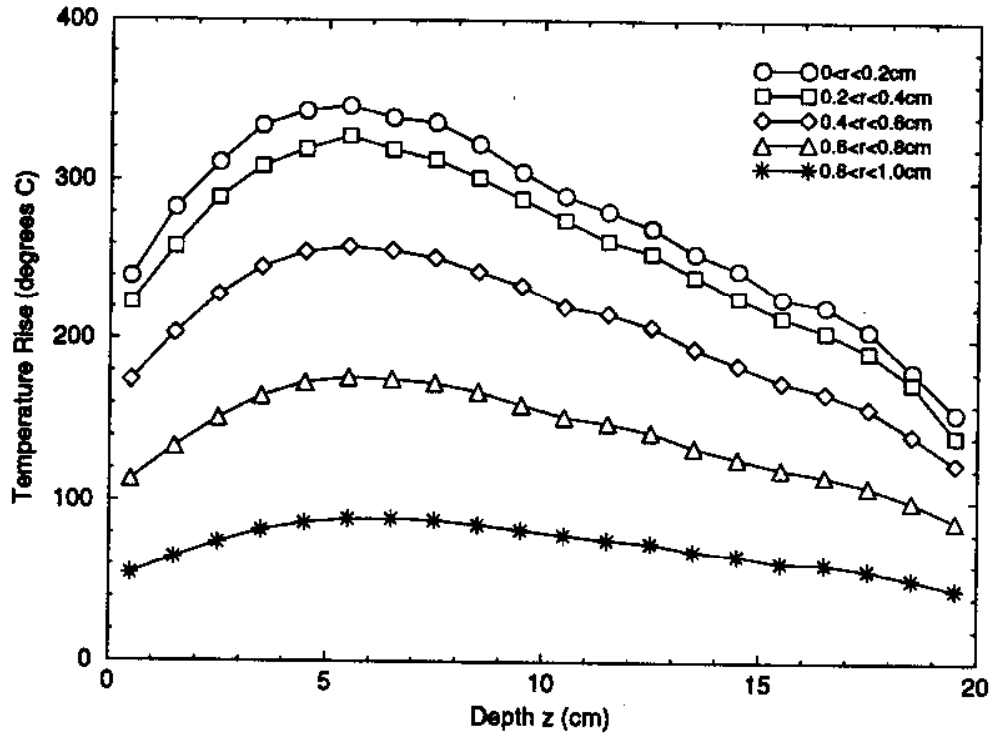

FIGURE 8. Equilibrium temperature rise Δ T relative to room temperature T_0=27°C in 1 cm radius copper target after 60th pulse (t=2 sec). Target is irradiated by 8 GeV beam of 5×10^{13} protons at 30 Hz.

Solenoid Heating

Energy deposition in the primary 28 Tesla solenoid resulting from the intense radiation environment around the target might cause quenching. Based on hybrid designs reported in the literature, the solenoid is nominally assumed to consist of a normal-conducting 'insert', starting at 7.5 cm radius, and a superconducting 'outsert' starting at 30 cm. The latter will quench if the heat load becomes excessive. Fig. 9 shows average power density as a function of radius for 5×10^{13} protons at 30 Hz on a 1.5 λ_I Cu target. The end of the target coincides with the end of the primary solenoid. As expected, power density is highest at the downstream end of the solenoid (z=22.5 cm in this case). It is lower everywhere for lower Z targets. At 30 cm radius—where the superconducting solenoid starts—the power density is 4.5 mW/g which is below the experimentally determined quench limit of about 8 mW/g for Tevatron dipoles.

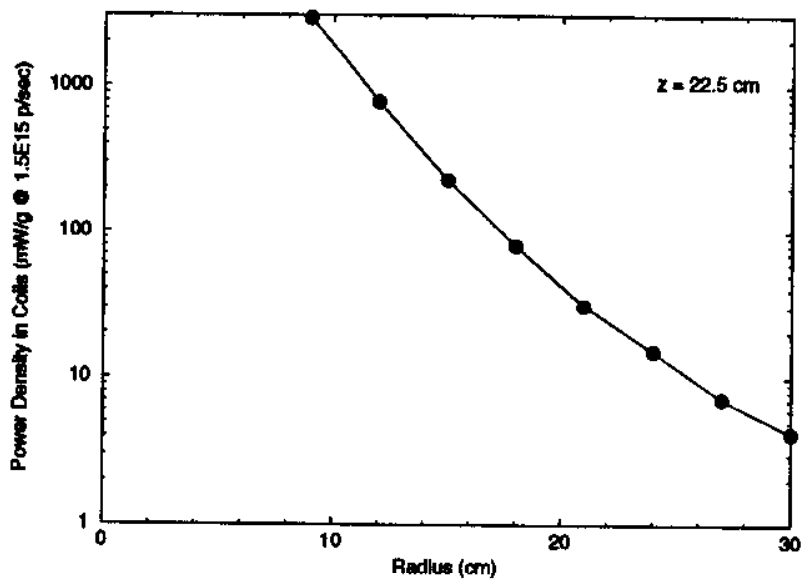

FIGURE 9. Peak power density in solenoid superconducting coils as a function of radius due to particle debris from 1.5 λ_I copper target irradiated by 8 GeV beam of 5×10^{13} protons at 30 Hz.

PION AND MUON COLLECTION

Particles produced in the target are transported along a beamline which forms the first stage of muon collection and acceleration en route to the collider. Attention must also be paid at this point to disposal of the other non-μ-producing particles, mostly nucleons, $e^{\pm}$, and γs. At a minimum such a beamline involves some focusing of the produced pions and their muon progeny just to keep them from being lost on the walls. Then, when an optimum population is reached, the muons are cooled and accelerated. More ambitious (and probably more realistic) schemes may begin cooling and/or acceleration earlier. But in this early phase of the study it is perhaps best to leave these more ambitious schemes for future consideration. This section thus concentrates only on the muon collection aspects of the post-target beamline. Even in this limited domain there appears a rich variety of strategies of which only a few are examined here.

Particle Decay

Pions and kaons immediately begin decaying into muons downstream of the target ($\lambda_\pi = 56\,p$, $\lambda_K = 7.5\,p$, and $\lambda_\mu = 6233\,p$ where λ is in meters and p in GeV/c). Particles that do not intercept the walls in their first Larmor gyration typically are transported down the entire 7 T channel. The vast majority of lost particles are wiped

out in the first 15 meters. This straight collection channel (without RF debuncher cavities in the simulation) is quite efficient with only 40% of all muon-producing particles lost on the walls and close to 60% yielding transported muons.

While decay is fully incorporated into the simulations a few qualitative remarks may help interpret results. Only $\pi \rightarrow \mu\nu$ and $\mu \rightarrow e\nu\overline{\nu}$ decays are of real importance to this problem. Kaons are practically negligible as a source of muons in the present context: (1) their total yield is only about a tenth that of pions, (2) their branching ratios to muons are somewhat less favorable and (3) the decay kinematics produces muons typically with much larger $p_\perp$ than do pions. When they are included in a full simulation it is seen that only about 1% of all muons in the accepted phase space are due to kaons.

As a function of distance traversed along the pipe, z, pions decay to muons at a rate

$$dN_\pi/dz = \frac{1}{\lambda_\pi} e^{-z/\lambda_\pi} \tag{4}$$

where $\lambda_\pi = p_z^\pi \tau_\pi / m_\pi$ and m_π, τ_π, and p_z^π are pion mass, lifetime, and momentum along the pipe axis. There is a similar equation for muons. From the decay laws of radioactive chains, the fraction of muons at z is given by

$$N_\mu/N_\pi = \frac{\lambda_\mu}{\lambda_\mu - \lambda_\pi}\left(e^{-z/\lambda_\mu} - e^{-z/\lambda_\pi}\right). \tag{5}$$

From Eqn. (5) the maximum muon yield is realized at

$$z_{opt} = \frac{1}{\lambda_\pi - \lambda_\mu} \ln \frac{\lambda_\pi}{\lambda_\mu}. \tag{6}$$

To arrive at a more concrete (but approximate) estimate of z_{opt}; p_z^μ is replaced by its average value

$$\overline{p_z^\mu} = \frac{m_\pi^2 + m_\mu^2}{2m_\pi^2} p_z^\pi \simeq 0.785 p_z^\pi. \tag{7}$$

When inserted into Eqn. (6) this results in

$$z_{opt} \simeq 251 p_z^\pi \tag{8}$$

in meters with p_z^π in GeV/c. Eqn. (5) then indicates that at z_{opt} the number of muons per pion produced at the target is about 0.95.

For a *spectrum* of pions, optimization of z requires folding Eqn. (7) with the p_z^π of the spectrum. But even without such a folding, a rough knowledge of the spectrum establishes a distance scale for the decay channel. It also follows that for a spectrum 0.95 μ/π must be regarded as an upper limit. Since at distances of order z_{opt} and beyond most pions have decayed, the muon yield is governed by the muon decay length and one expects a broad maximum (at a z_{opt} corresponding roughly to the peak p_z^π of the spectrum produced at the target) where the theoretical maximum

of 0.95 μ/π should be close to being realized. Taking 0.5 GeV/c as a characteristic pion momentum for the distribution, one expects the muon population to reach a maximum about 125 meters downstream of the target and fall off slowly after that. For a uniform distribution in the range 0.25–0.75 GeV/c a maximum 0.94 μ/π is attained at 130 m. Fig. 10 shows muon yield per proton versus distance from a simulation with a 22.5 cm long copper target. In this case the maximum yield is 0.52 μ^+ and 0.34 μ^- per 8 GeV proton.

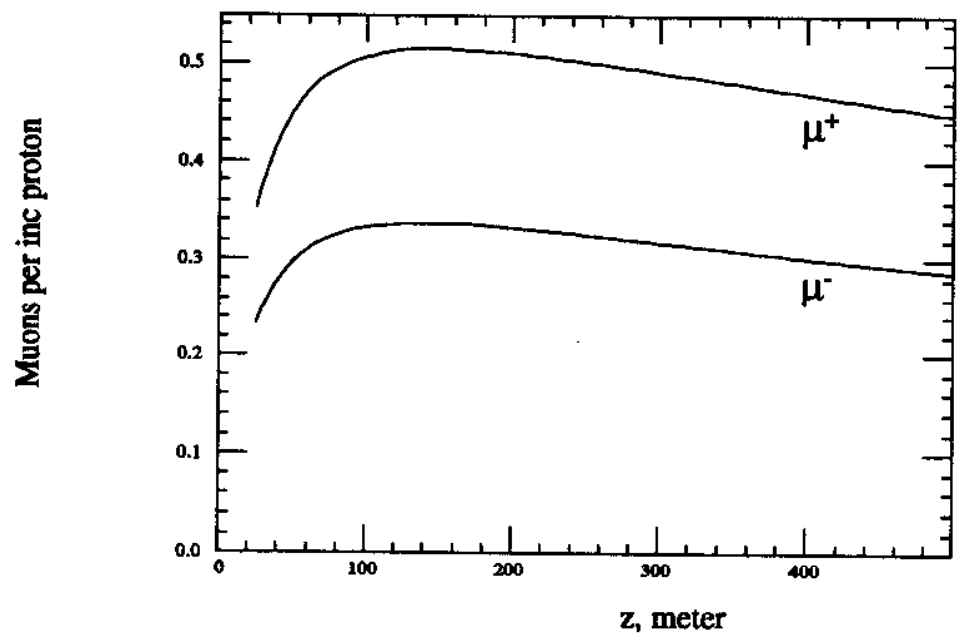

FIGURE 10. Muon yield vs distance from target for 22.5 cm copper target and standard straight decay solenoid.

Beam Collection in a Straight Solenoid

The transverse emittance of the nascent muon beam is of practical interest in the design of the downstream muon cooling channel and its required acceptance. Fig. 11 shows muon beam fractional contours in x or y transverse phase space 150 meters downstream of the target. The plot shows the fraction (in steps of 0.1) of the beam within the indicated x and $x' = p_x/p$ limits independent of y and y'. Plots for positive and negative muons are nearly identical. Note that the muon beam is well localized transversely in a channel with emittance $\epsilon_x(90\%) = 4.5 \times 10^{-2}$ meter, $|x| \leq 10$ cm and $|x'| \leq 0.45$. In the absence of x-y correlations, 81% of the muon beam is contained within both the $\epsilon_x(90\%)$ and $\epsilon_y(90\%)$ contours. For reference note that $\epsilon_x(30\%) = 5.4 \times 10^{-3}$ meter and $\epsilon_x(60\%) = 1.6 \times 10^{-2}$ meter.

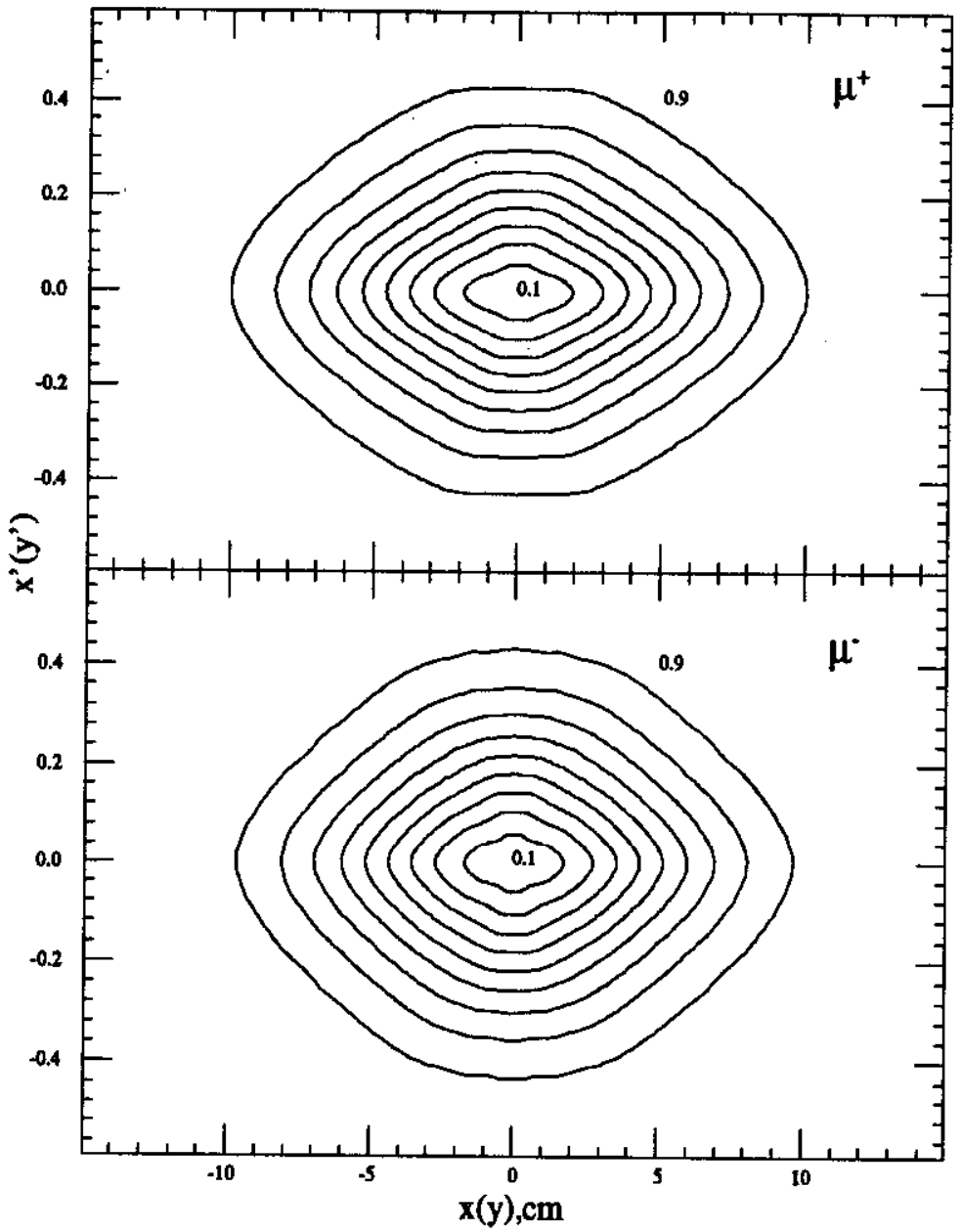

FIGURE 11. Contours of relative fractional transverse emittance for μ^+ (top) μ^- (bottom) in steps of 0.1, e. g., innermost contour contains 10 % of all muons.

Muon yield as a function of momentum is of particular interest in designing an RF system to reduce the momentum spread. Figs. 12(a–c) display momentum spectra of μ^+ from a copper target within the 0.3, 0.6, and 0.9 x and y emittance contours (cfr. Fig. 11). Figs. 13(a–c) present the corresponding μ^- spectra. Total number of muons per proton within the indicated contours are shown in parentheses. As expected, muons with small transverse emittance tend to have somewhat higher momenta. These plots quantify the trade-off in yield between momentum spread and transverse emittance. For example, the spectra of Figs. 12c or 13c each contain 81% of all μ^+ and μ^-, respectively. About 60% of this beam is contained in the momentum range 0.22 to 0.72 GeV/c corresponding to $\Delta p/p = \pm 0.53$ and $|\Delta v/c| = 0.075$. This constitues a relatively high density muon beam which contains a total of 0.26 μ^+/p and 0.17 μ^-/p. These plots characterize the raw muon beam and help provide insight for the design of a cavity system to debunch the parent pion beam. As stated earlier, this is not as yet included in the simulation.

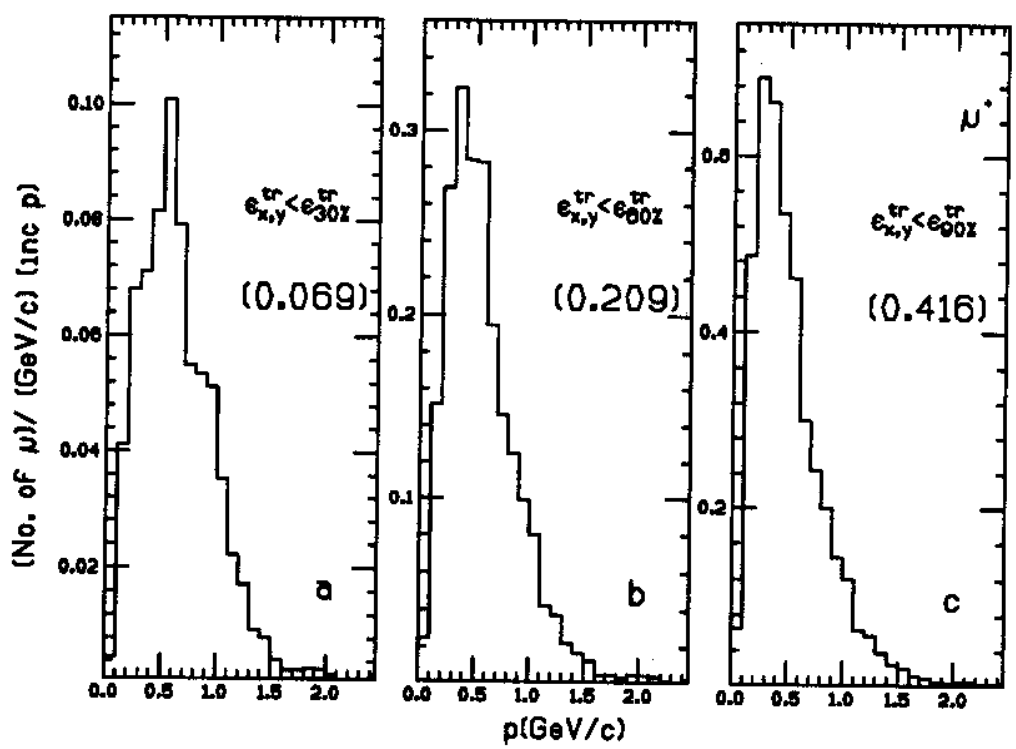

FIGURE 12. Momentum spectra of positive muons 150 m downstream within indicated transverse emittance. Totals in parentheses.

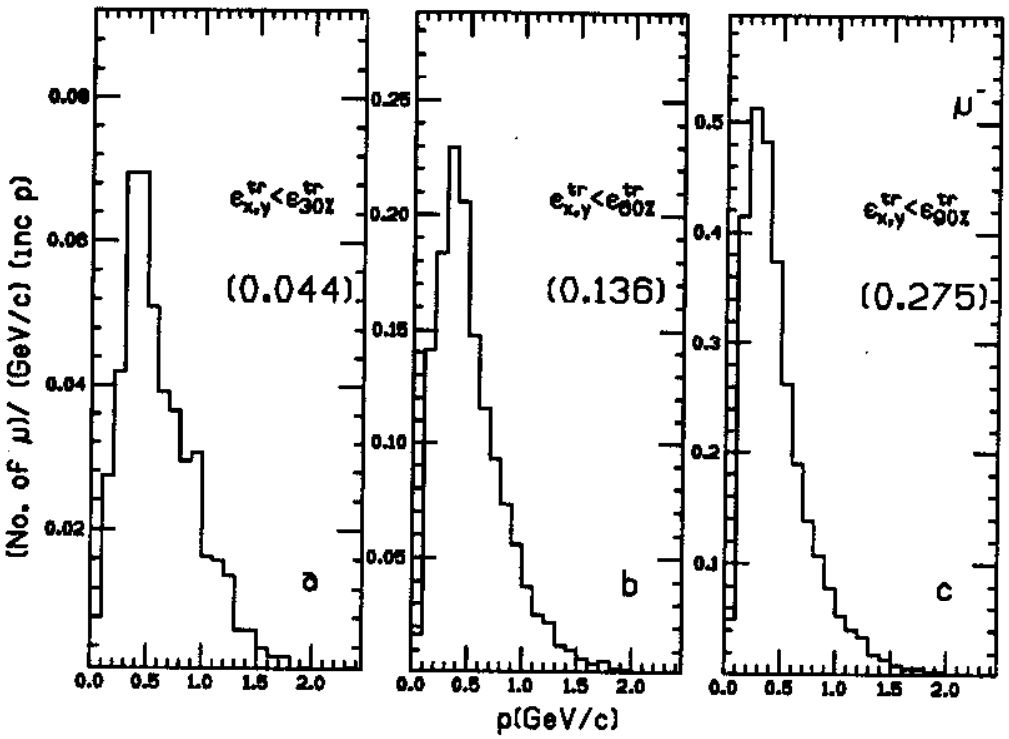

FIGURE 13. Momentum spectra of negative muons 150 m downstream within indicated transverse emittance. Totals in parentheses.

For each proton bunch on target an intense pulse of mostly protons, electrons, pions, kaons and muons starts down the 7 T solenoid channel. Neutrals like photons and neutrons are unaffected by the magnetic field and are lost onto the walls according to their initial trajectory. Fig. 14 shows particle densities as a function of time at the beginning of the decay channel. Total number of muons per proton of each species are indicated in parentheses. These distributions do not include the time spread of the proton beam. The latter—which depends on the design of the proton driver—is readily folded into the results of Fig. 14 at any stage in the simulation (prior to the RF cavities). When this pulse arrives at a debuncher cavity (proposed to reduce particle momentum spread) particles of the wrong sign relative to the electromagnetic wave would actually become bunched, with an increase in their momentum spread. Most such particles would quickly be lost downstream in any magnetic bend.

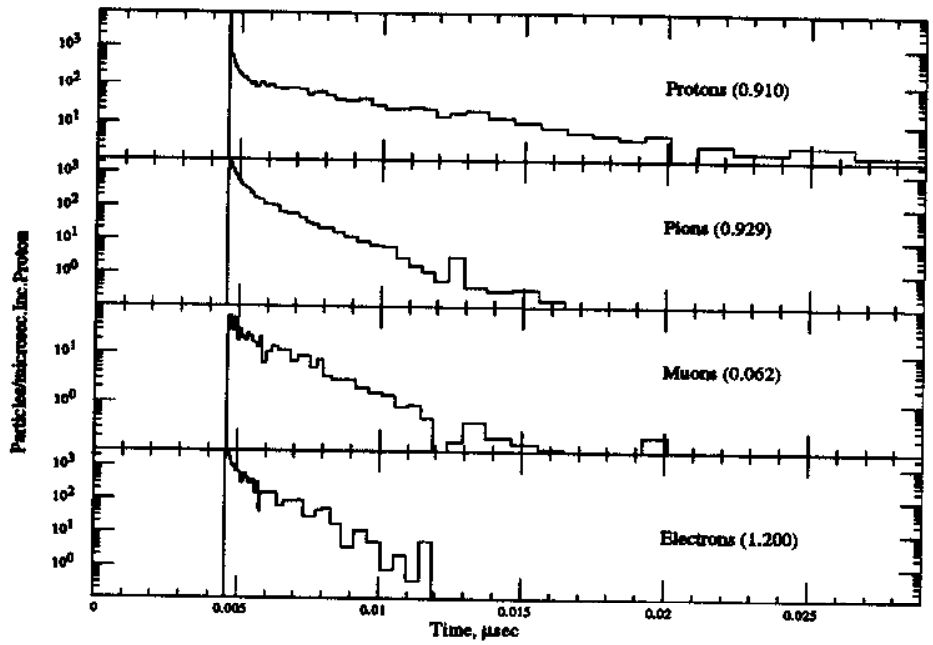

FIGURE 14. Particle densities as a function of time at end of matching region (1.15 m after end of target).

Curved Solenoid for Beam Separation

The proposed straight-solenoid plan uses two separate proton bunches to create separate positive and negative muon bunches accepting the loss of half the muons. In addition the debuncher cavities have to contend with a large population of protons, electrons and positrons that will tend to mask the desired π/μ bunches. Great advantage may be gained if the pions can be charge-separated as well as isolated from the bulk of protons and other charged debris before reaching the cavities. For the same number of proton bunches on target, a scheme which permits charge separation would produce a gain of a factor of two in luminosity. By coalescing the two proton bunches, this becomes a factor of four with little effect on target heating or integrity.

The solenoid causes all charged particles to execute Larmor gyrations as they travel down the decay line. As is well known from plasma physics, a gradient in the magnetic field or a curvature in the field produces drifts of the particle guide centers. Drift directions for this case are opposite for oppositely charged particles. Drift velocities depend quadratically on particle velocity components. This is exploited here by introducing a gentle curvature to the 7 T decay solenoid.

In the decay line, most particles moving in the curved solenoid field have a large velocity parallel to the magnetic field (v_z of order c) and a smaller perpendicular

velocity ($v_\perp \simeq 0.3$ c or less) associated with their Larmor gyration. In the curved solenoid the v_s motion gives rise to a centrifugal force and an associated 'curvature drift' perpendicular to both this force and the magnetic field. The field in the curved solenoid also has a gradient (field lines are closer near the inner radius than near the outer radius) resulting in an added 'gradient drift' in the *same* direction as the curvature drift. Averaged over a Larmor gyration, the combined drift velocities can be written as [8]

$$\vec{v}_R + \vec{v}_{\nabla B} = \frac{m\gamma}{q}\frac{\mathbf{R}\times\mathbf{B}}{R^2B^2}(v_s^2 + \frac{1}{2}v_\perp^2), \tag{9}$$

where $m\gamma$ is the relativistic particle mass, q the particle charge, and R is the radius of curvature of the solenoid with central field B. Note that in the present application the curvature drift ($\propto v_s^2$) is typically much larger than the gradient drift ($\propto v_\perp^2/2$). This is in contrast to a plasma where these contributions are comparable.

The drift velocity changes sign according to charge so positive and negative pions become transversely separated. For unit charge and for $\mathbf{R} \perp \mathbf{B}$ the magnitude of the drift velocity can be written in convenient units as

$$\beta_d = \frac{E\left(\beta_s^2 + \frac{1}{2}\beta_\perp^2\right)}{0.3RB}, \tag{10}$$

where E is particle energy in GeV, R is in meters and B in Tesla. The total drift displacement, D, experienced by a particle moving for a distance, s, along the field follows immediately from Eqn. (10)

$$D = \frac{1}{0.3B}\frac{s}{R}\frac{p_s^2 + \frac{1}{2}p_\perp^2}{p_s} \tag{11}$$

with D in meters, B in Tesla and momenta in GeV/c. Note that only the *ratio* s/R appears in Eqn. (11) which corresponds to the angle traversed along the curved solenoid. A typical 0.5 GeV pion ($p_\perp \ll p_s$) in a 7 T solenoid with R = 25 m has a drift velocity of about $10^{-2}c$. After moving 20 meters downstream in the solenoid, a 0.5 GeV positive and negative pion should be separated by about 35 cm.

The present study considers only *circularly* curved solenoids. Here the curvature and the $\nabla\times\boldsymbol{B}= 0$ condition requires the field, which is nonzero only along ϕ (i.e. along the axis of the curved beampipe) to have a $\frac{1}{R}$-dependence. This is readily incorporated in the detailed step-by-step simulations. Fig. 15a shows the pion distributions 20 m downstream of the target (which is in a 28 T field) calculated for a curved solenoid geometry. The centroid separation agrees well with what is expected from the drift formula. Also as expected, higher energy pions are shifted farther and low energy pions less. Decay muons created up to this point are separated by a comparable margin (Fig. 15b). At this point one could place a septum in the solenoid channel and send the two beams down separate lines to their own debunching cavities.

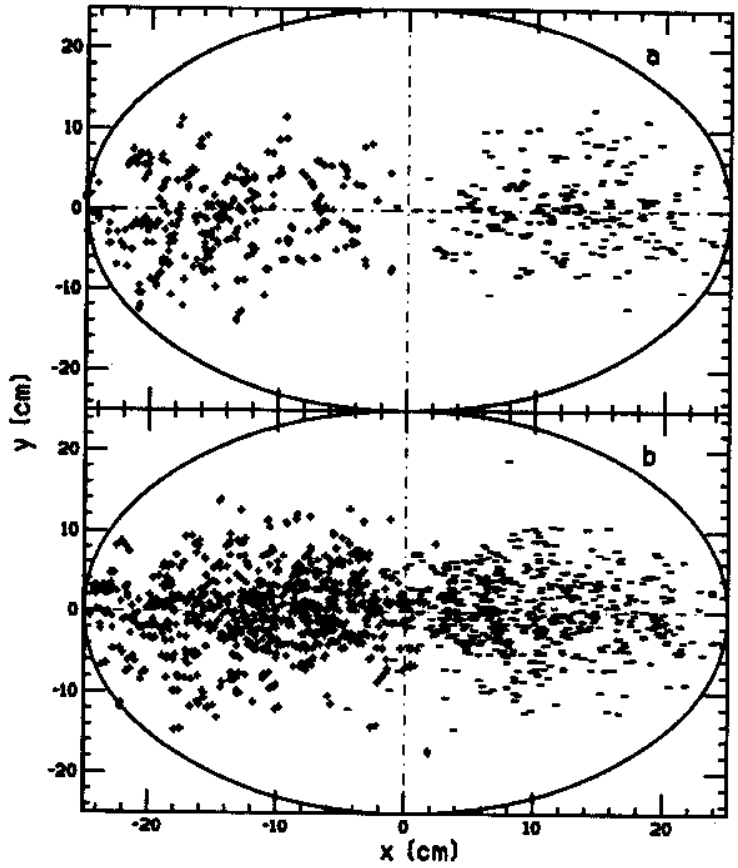

FIGURE 15. Position of (a) π^+ and π^-, and (b) μ^+ and μ^- 20 m downstream along curved solenoid (inner radius a=25 cm, R=25 m, B=7 T).

The curved solenoid also serves well to rid the beamline of neutral particles and most of the remnant protons after the target. Neutrals like photons and neutrons intercept the curved solenoid with their straight trajectories and deposit their energy over a large area. Beam protons which underwent little or no interaction in the target have such large forward momenta that they are unable to complete one full gyration before intercepting the curved wall downstream. Hence Larmor-averaged drift formulae cannot be applied. Fig. 16 provides some snapshots of this tight proton bunch moving away from the lower energy protons at successive downstream locations. At four meters downstream all beam-like protons have intercepted the wall. Protons remaining in the pipe for long distances have momenta similar to the positive pions and thus will accompany them downstream. Roughly 0.7 protons per positive pion/muon are still in the pipe at 10 meters which should not overburden the debuncher cavities with extraneous beam. Electrons and positrons have typically much lower momenta than pions and muons. Simulations indicate that they do not drift far from the curved solenoid axis and most would be lost at the septum.

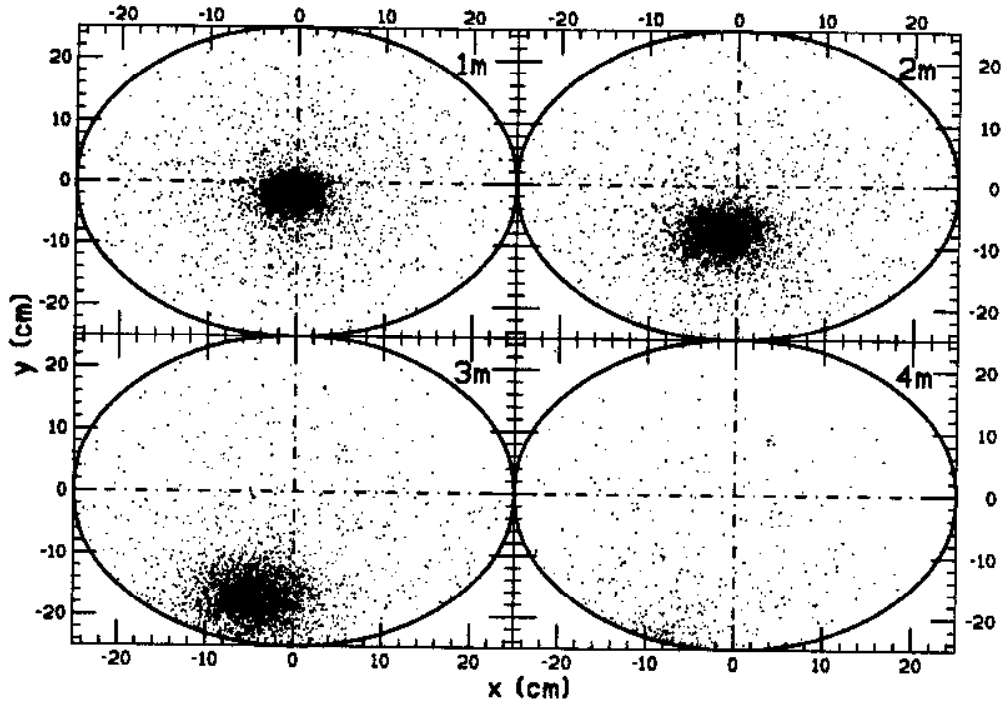

FIGURE 16. Scatter plot of x,y coordinates of protons above 5 GeV while traversing curved solenoid. Distance along center of curved solenoid is in upper right hand corner.

For the same diameter pipe the broadening associated with charge separation in the curved solenoid leads to increased particle losses on the walls compared with the straight case. An increase in pipe diameter is thus very desirable. To optimize the geometry with respect to yield would require many simulation runs. Since the curved regions may extend over long distances, this leads to much longer computation times for detailed step-by-step simulations to the point of becoming prohibitive when exploring a large parameter space. For survey type calculations a simplified procedure was therefore adopted.

The procedure adopted is then that for each pion encountered while reading a MARS file: (1) the position vector of the Larmor guide center is determined, to which (2) the drift displacement vector **D** is added, with appropriate sign, along the direction perpendicular to **B** and **R**. It is then determined whether (3) the entire Larmor circle fits inside the *half*-aperture appropriate to its charge, i.e., the side in the direction of the drift. More precisely, this last condition is $r_g < a - r_L$ and $\pm x_g > r_L$ where r_L is the Larmor gyration radius, a is the pipe radius and subscript $_g$ refers to the final guide center position with the sign of x_g dependent on particle charge. If a pion meets these criteria it is assumed to contribute to the yield. Decay of pions or muons is omitted from consideration. This was justified above (cfr. Particle Decay).

The study of pion/muon yield in a circularly curved beampipe (starting immediately after the target) with *constant* central field can thus be reduced to a problem with just three parameters B, s/R, and a. Some sensible range of values can thus be readily explored over a reasonably dense grid. An optimization based on yields alone is perhaps somewhat unrealistic. A measure of how effectively one can separate the two components into different beamlines is provided by computing the centroid of each distribution as well as its *rms* radius. Computation is very fast and readily repeated for different sets of parameters to perform a more complete optimization.

A more realistic scenario starts with a 28 T field surrounding the target followed by a *curved matching region* which accomplishes simultaneously both transition to lower field and charge separation. The changing field causes an adiabatic decline in $p_\perp$ according to

$$p_{\perp f}^2 = p_{\perp i}^2 \frac{B_f}{B_i} \tag{12}$$

along with a correponding change in p_s so as to conserve total p. Subscript i refers to initial and f to final values of B and $p_\perp$, i.e., those prevailing at S, the total distance along the central field line. Ignoring the other field components—due to the declining field, cfr. Eqn. (3)—the total drift becomes

$$D = \int v_D dt = \int v_D \frac{ds}{v_s} = \int_0^S \frac{1}{300BR} \frac{p_s^2 + \frac{1}{2}p_\perp^2}{p_s} ds, \tag{13}$$

where now B, p_s and $p_\perp$ all depend on s. Assuming a *linear* decline of the central field $B = B_i(1 - as)$, and the dependence of p_s and $p_\perp$ on s this entails, one obtains

$$D = \frac{S}{300(B_i - B_f)R} p_0 \left[\ln \frac{(p_0 - p_{sf})(p_0 + p_{si})}{(p_0 + p_{sf})(p_0 - p_{si})} + p_{sf} - p_{si} \right], \tag{14}$$

where p_0 is the total momentum of the pion.

Thus for fixed B_i the problem remains confined to three parameters: B_f, S/R, and a. Note also that the Larmor radius changes with s here. Fig. 17a shows $\pi^+\mu^+$ yield in a curved solenoid with a constant 50 cm pipe radius for different values of the final magnetic field at the end of the matching region for a 22.5 cm long copper target. Eqn. (13) can also be applied to a field having the $B_0/(1 + \alpha s)$ dependence. Again an expression for D, though somewhat lengthier than Eqn. (14), is readily obtained and again the problem remains one of the same three parameters. For comparison, Fig. 17b shows $\pi^+\mu^+$ yield for the $1/(1 + \alpha s)$ field dependence with everything else as in Fig. 17a. Note that the yields peak at somewhat smaller s/R.

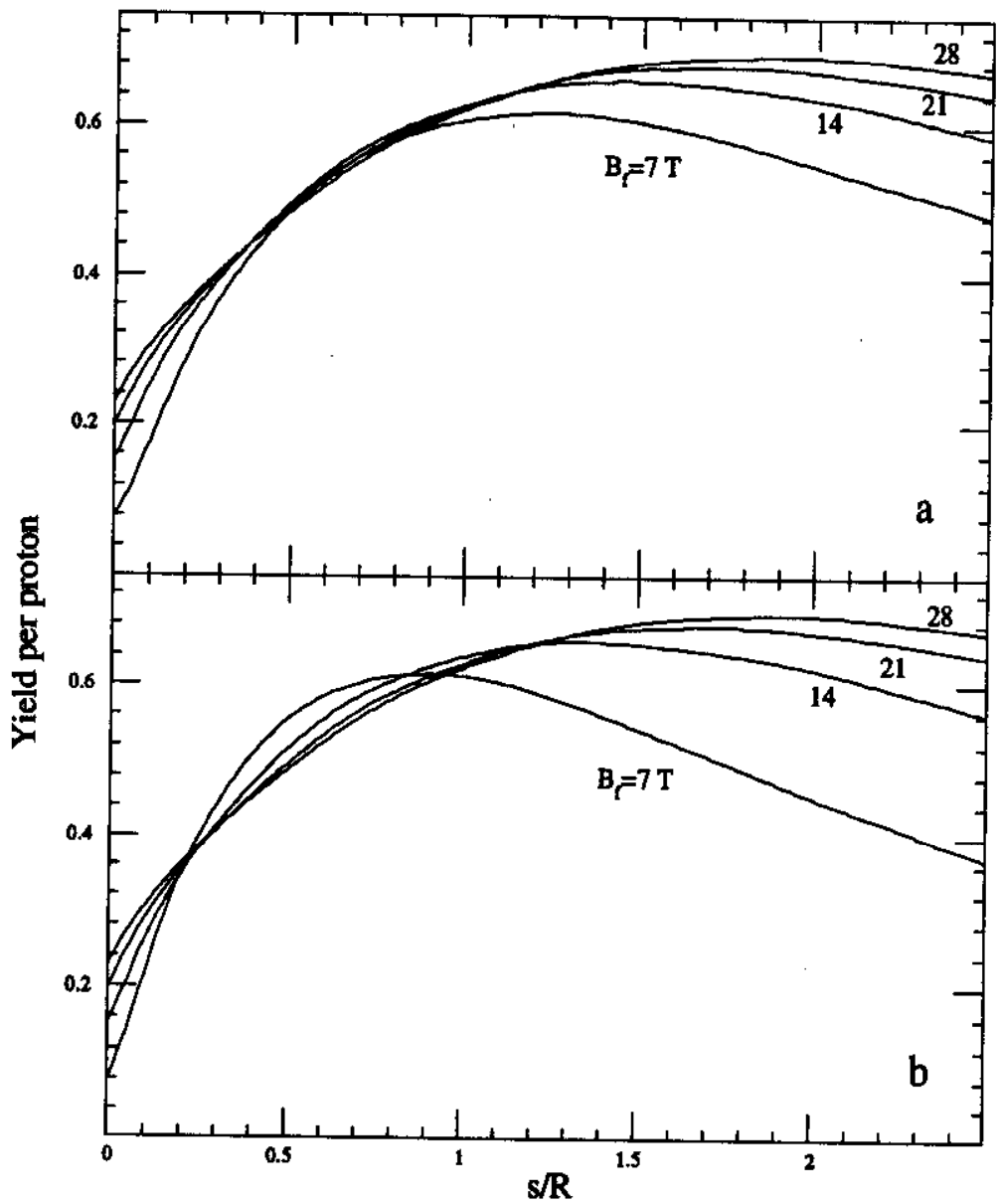

FIGURE 17. (a) Yield of positive pions and muons vs s/R for 22.5 cm copper target in straight solenoid with $B_0 = 28$ T followed by curved solenoid with $B = B_0(1 - \alpha s)$. Labels indicate final B reached at s/R. (b) Same for $B = B_0/(1 + \alpha s)$ in curved solenoid.

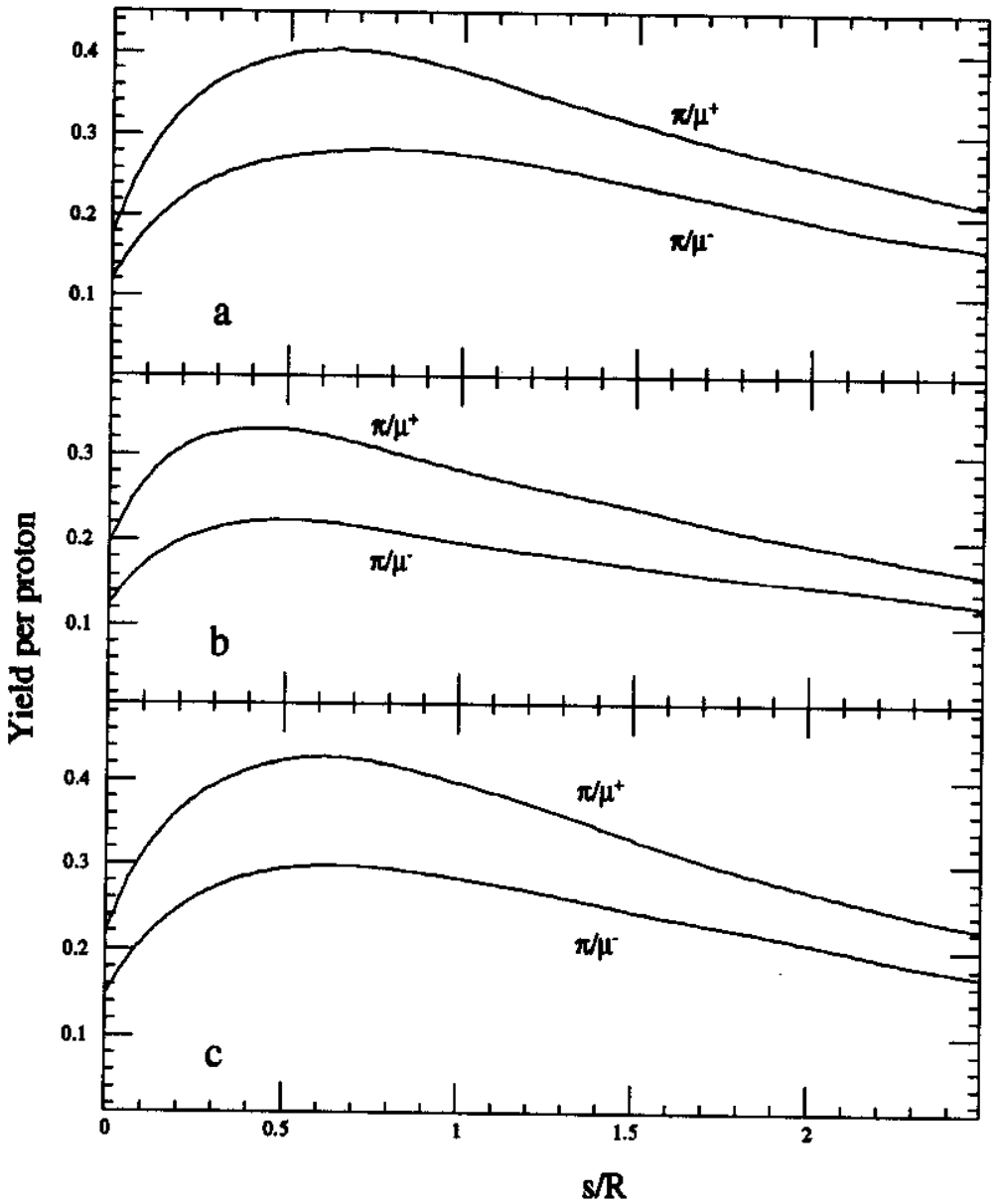

FIGURE 18. (a) Yield vs s/R for 22.5 cm copper target in solenoid of 7 T throughout. (b) Same for 57 cm carbon target. (c) Same for 30 cm copper target.

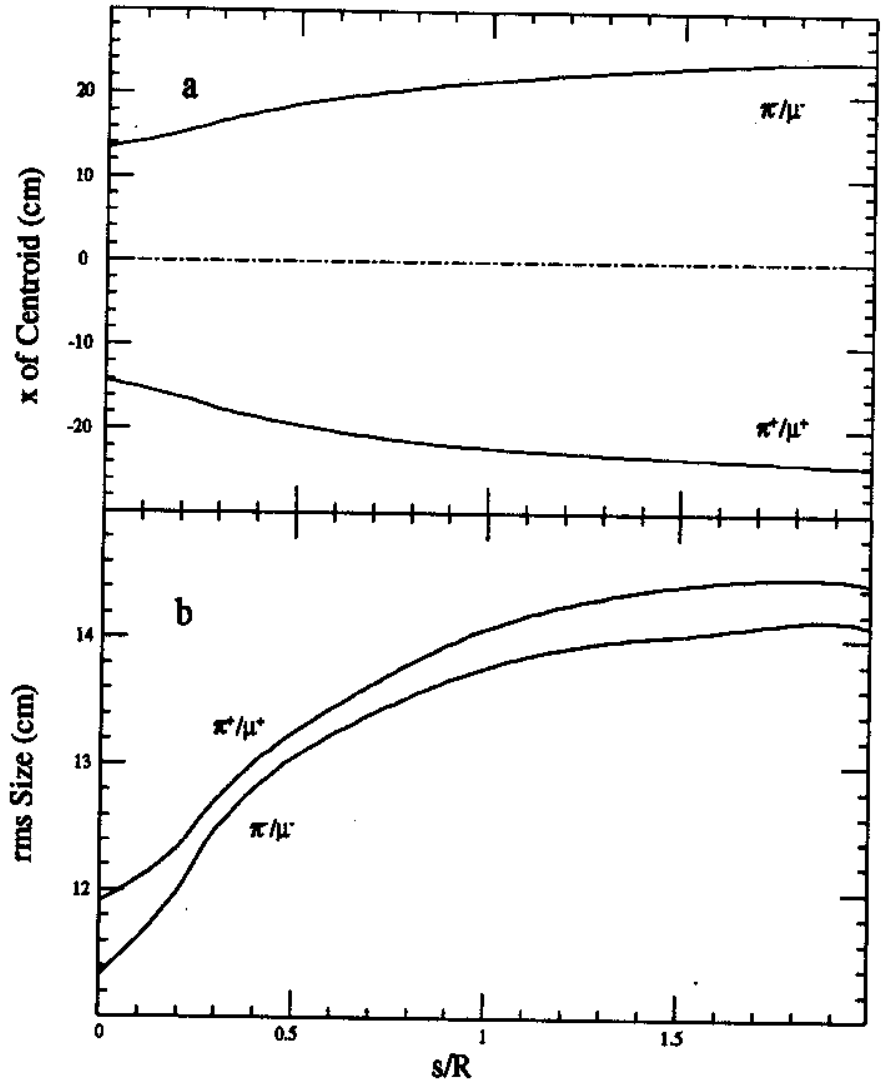

FIGURE 19. (a) Distance of centroid to magnet center vs s/R for 22.5 cm copper target, 7 T, r=50 cm solenoid throughout. Note beampipe extends beyond graph. (b) rms size of each beam vs s/R.

Because of the advanced magnet technology required for very high field (> 15T) solenoids, it is of interest to investigate yields obtained when lower magnetic fields prevail throughout the entire geometry. To keep matters simple a constant 7 T field and 50 cm solenoid radius is assumed—which might be considered state-of-the-art [9]. The solenoid is straight for the target portion, then curves to affect the desired charge separation, then straightens again to form the decay channel. In this last portion separation of plus and minus beams at a septum is to take place but details of this implementation are not considered here. Such a solenoid has a transverse momentum acceptance of 0.52 GeV/c and a normalized phase space acceptance of 1.87 m·rad. Fig. 18a,b show $\pi\mu$ yields for this type solenoid and for $1.5\lambda_I$ copper

and carbon targets, respectively. Fig. 18c presents the yield curves for the copper target when the length is increased to $2\lambda_I$, suggesting longer targets to be better for this geometry. Yields are presented as a function of s/R and it is thus advantageous to begin the straight (decay) portion of the pipe in the region near the maxima. Fig. 19a,b show respectively the centroid position of the plus and minus beams within the beampipe and their *rms* size for the standard copper target. The latter refers only to the distribution of the guide centers and excludes the spread due to the Larmor motion. Recall that both centroid and *rms* size refer only to those particles for which the entire Larmor circle fits inside the proper half-aperture. This accounts for the non-zero centroid positions at z=0.

CONCLUSIONS AND OUTLOOK

The choice of target shows that while a 1–2 λ_I of copper is optimum for yield, lower-Z targets are not much worse—about 20% depending on the collection geometry. Hence lower-Z targets, because of the lower energy deposition associated with them, may still be the targets of choice. Microchannel cooling and/or elliptical beams and targets may be used to deal with target heating problems. Quenching due to energy deposition in superconducting solenoids is a problem only for high-field/small-diameter magnets. Lower field solenoids with larger diameter are much less likely to quench and also pose less technological difficulties. While the yields associated with them are somewhat lower there may exist some reasonable trade-off.

The simulations confirm the superiority of muon collection with the solenoid scheme in this energy regime. Total yields of about 0.5 muons per proton of either charge appear to be obtainable. Considerations of π/μ decay indicate a collection limit of about 0.95 muons per pion. Kaons appear to contribute far less than their numbers to the usable muon flux and are practically negligible in this application. The pion momentum spectrum generated by 8 GeV protons peaks around 0.35 GeV/c. The collection system tends favor the lower energies and most muons are expected to be in the 0.2 to 0.5 GeV/c range. Charge separation by *curved* solenoids practically doubles the number of muons collected and appears to be beneficial in disposing of the host of unwanted particles generated in the target along with the through-going beam protons. Yields are sensitive to field strengths and solenoid diameter as well as to the s/R parameter—which indicates where to end the curvature and send the beams their separate ways.

As is evident from Eqns. (11) and (14), there exists a strong correlation between drift distance and momentum with the larger momenta experiencing the larger drift. This could be exploited for cooling purposes, e.g., after each beam is traveling in its own channel and most pions have decayed, a (cylindrically symmetric) wedge would clearly introduce some longitudinal cooling. Even some 'pion cooling' might be beneficial during the separation stage. This would be accomplished by intermittently placing collars near the perimeter. Such a collar would only affect high momentum (large drift velocity), high $p_\perp$ (large Larmor radius) pions. It is clear

that—unless a nuclear interaction occurs—some cooling results in both transverse and longitudinal space. Moreover the reduction in $p_\perp$ shrinks the pion's Larmor radius and tends to move its guide center in the general direction of the drift. The new Larmor circle is thus more likely to fit entirely into proper half-aperture of the beampipe with improved subsequent capture probability. The reduction in p_s reduces the drift velocity which might prevent some pions from being lost on the walls. Some of these benefits are offset by pions undergoing nuclear interaction or large angle scattering—although some salvagable pions might yet emerge from such events.

A definitive optimization of muon production and collection best awaits further studies of muon cooling and acceleration. Only when it is known—at least approximately—how to mesh these functions with the parts explored in this paper can one proceed reasonably efficiently towards this goal. But cooling and acceleration, in turn, depend strongly on the particulars of muon production and collection. This study thus provides a necessary step in the iteration which—it is hoped—eventually will lead to a realistic design of a muon collider.

References

[1] Palmer, R., Proc. 1st $\mu^+\mu^-$ Collider Workshop, Napa, CA (1992), in *Nucl. Inst. Meth.* **A350**, 24–56 (1994).

[2] Noble, R., Proc. 3rd Int. Workshop on Advanced Accelerator Concepts, Port Jefferson, NY, AIP Conf. Proc. **279**, p. 949 (1993).

[3] Palmer, R., et al., "Monte Carlo Simulation of Muon Production", BNL–61581 (1995).

[4] Mokhov, N. V., "The MARS Code System User's Guide, Version 13 (95)", Fermilab FN–628 (1995).

[5] See e.g., Montanet, L. et al., "Review of Particle Properties", *Phys. Rev.* **D50**, 1177 (1994).

[6] Jackson, J. D., *Classical Electrodynamics*, 2nd Ed., J. Wiley, New York, 1975.

[7] "ANSYS (rev. 5.1)", Swanson Analysis System, Inc., SASI/DN–P511:51, Houston (1994).

[8] Chen, F. F., *Introduction to Plasma Physics*, Plenum, New York, pp. 23–26 (1974).

[9] Green, M., "Pion Capture Magnet System", presented at 9th Adv. ICFA Beam Dynamics Workshop, Oct. 1995, Montauk, NY.